A&A 562, A138 (2014)
DOI: 10.1051/0004-6361/201322236
© ESO 2014

Astronomy & Astrophysics

Reconstructing the density and temperature structure of prestellar cores from *Herschel* data: A case study for B68 and L1689B⋆

A. Roy[1], Ph. André[1], P. Palmeirim[1], M. Attard[1], V. Könyves[1,2], N. Schneider[1,3], N. Peretto[1,4], A. Men'shchikov[1], D. Ward-Thompson[5], J. Kirk[5], M. Griffin[4], K. Marsh[4], A. Abergel[2], D. Arzoumanian[2], M. Benedettini[6], T. Hill[1,7], F. Motte[1], Q. Nguyen Luong[8], S. Pezzuto[6], A. Rivera-Ingraham[9,10], H. Roussel[11], K. L. J. Rygl[6], L. Spinoglio[6], D. Stamatellos[5], and G. White[12,13]

[1] Laboratoire AIM, CEA/DSM-CNRS-Université Paris Diderot, IRFU/Service d'Astrophysique, C.E. Saclay, Orme des Merisiers, 91191 Gif-sur-Yvette, France
e-mail: [Arabindo.Roy;philippe.andre]@cea.fr
[2] Institut d'Astrophysique Spatiale, CNRS/Université Paris-Sud 11, 91405 Orsay, France
[3] Université de Bordeaux, Laboratoire d'Astrophysique de Bordeaux, CNRS/INSU, UMR 5804, BP 89, 33271 Floirac Cedex, France
[4] School of Physics & Astronomy, Cardiff University, Cardiff CF29 3AA, UK
[5] Jeremiah Horrocks Institute, University of Central Lancashire, Preston PR1 2HE, UK
[6] INAF-Istituto di Astrofisica e Planetologia Spaziali, via Fosso del Cavaliere 100, 00133 Rome, Italy
[7] Joint ALMA Observatory, Alonso de Córdova 3107, Vitacura, Santiago, Chile
[8] Canadian Institute for Theoretical Astrophysics, University of Toronto, 60 St. George Street, Toronto, ON M5S 3H8, Canada
[9] Université de Toulouse, UPS-OMP, IRAP, Toulouse, France
[10] CNRS, IRAP, 9 Av. colonel Roche, BP 44346, 31028 Toulouse Cedex 4, France
[11] Institut d'Astrophysique de Paris, UMR7095 CNRS, Université Pierre & Marie Curie, 98 bis boulevard Arago, 75014 Paris, France
[12] Department of Physics and Astronomy, The Open University, Walton Hall, Milton Keynes MK7 6AA, UK
[13] RAL Space, STFC Rutherford Appleton Laboratory, Chilton Didcot OX11 0QX, UK

Received 9 July 2013 / Accepted 8 November 2013

ABSTRACT

Utilizing multiwavelength dust emission maps acquired with *Herschel*, we reconstruct local volume density and dust temperature profiles for the prestellar cores B68 and L1689B using an inverse-Abel transform-based technique. We present intrinsic radial dust temperature profiles of starless cores directly from dust continuum emission maps disentangling the effect of temperature variations along the line of sight, which were previously limited to the radiative transfer calculations. The reconstructed dust temperature profiles show a significant drop in the core center, a flat inner part, and a rising outward trend until the background cloud temperature is reached. The central beam-averaged dust temperatures obtained for B68 and L1689B are 9.3 ± 0.5 K and 9.8 ± 0.5 K, respectively, which are lower than the temperatures of 11.3 K and 11.6 K obtained from direct SED fitting. The best mass estimates derived by integrating the volume density profiles of B68 and L1689B are 1.6 $M_{\odot}$ and 11 $M_{\odot}$, respectively. Comparing our results for B68 with the near-infrared extinction studies, we find that the dust opacity law adopted by the HGBS project, $\kappa_{\lambda} = 0.1 \times \left(\frac{\lambda}{300\ \mu\mathrm{m}}\right)^{-2}$ cm^2 g^{-1} agrees to within 50% with the dust extinction constraints.

Key words. stars: formation – submillimeter: general – ISM: individual objects: B68 – ISM: individual objects: L1689B – dust, extinction

1. Introduction

Recent submillimeter observations with the *Herschel* Space Observatory (Pilbratt et al. 2010) and particularly the results obtained as part of the *Herschel* Gould Belt Survey (HGBS; André et al. 2010) have significantly improved our global understanding of the early stages of low-mass star formation. It is now becoming clear that the formation of prestellar cores is intimately related to the ubiquitous filamentary structure present in the cold interstellar medium (ISM; Arzoumanian et al. 2011). On one hand one of the main objectives of the HGBS is to measure the prestellar core mass function (CMF) in nearby cloud complexes and to clarify the relationship between the CMF and the stellar initial mass function (IMF) on the other hand we also look at the link with the structure of the ISM (cf. Könyves et al. 2010; André et al. 2010, for preliminary results).

An accurate determination of the prestellar CMF requires reliable estimates of core masses. In the context of the HGBS project, core masses are derived from dust continuum emission maps obtained with *Herschel* between 160 μm and 500 μm. Dust emission is almost always optically thin at these wavelengths and can thus act as a surrogate tracer of the total (gas + dust) mass along the line of sight (LOS). This requires an assumption about the dust opacity in the submillimeter regime and reliable estimates of the dust temperature, $T_{\rm d}$. *Herschel* multiwavelength data can be used to estimate $\langle T_{\rm d} \rangle_{\rm LOS}$ through single-temperature greybody fits to the observed spectral energy distributions (SEDs; cf. Könyves et al. 2010). A complication,

⋆ Appendices are available in electronic form at http://www.aanda.org

however, is that such fits only provide the average temperature along the LOS and do not account for temperature gradients within the target sources. This is potentially a very significant problem when studying self-gravitating starless (or protostellar) cores with stratified density structures heated by an external or internal radiation field. The central temperatures of cold, starless cores and sometimes their mass-averaged temperatures can be overestimated due to the relatively strong emission from the screen of warmer dust in the outer layers of the cores which bias core mass estimates to lower values (cf. Malinen et al. 2011). Likewise, temperature variations along the LOS may hamper the derivation of reliable density profiles for prestellar cores (e.g., Kirk et al. 2005; Ysard et al. 2012) using submillimeter emission maps (e.g., Kirk et al. 2005; Ysard et al. 2012). Radiative transfer calculations (e.g., Evans et al. 2001; Stamatellos et al. 2007) have been performed to predict the dust temperature profiles of starless cores whose outer surfaces are exposed to heating by the local interstellar radiation field (ISRF). These calculations generally find a significant drop in $T_{\rm d}$ at the center of starless cores, but the actual magnitude of this temperature drop remained poorly constrained observationally before the advent of *Herschel* (see Ward-Thompson et al. 2002 for early results with ISO, however).

Here, we use *Herschel* observations to quantify the dust temperature gradient within two well-studied starless cores, B68 and L1689B. We introduce a simple yet powerful inversion technique based on the Abel integral transform to simultaneously reconstruct the 3D density and dust temperature profiles of dense cores by using the inputs of *Herschel* maps in four bands between 160 μm and 500 μm (also see Marsh et al. 2014 for an independent approach of solving similar problem). The basic goal of the present paper is to demonstrate the performance of the Abel inversion technique. We apply our algorithm to B68 and L1689B and compare the results with previous infrared extinction/absorption studies, which allow us to validate the dust opacity assumption made in earlier HGBS papers. We also test our technique on synthetic core models with known density and temperature profiles. While the method assumes spherically symmetric cores, we show that it yields satisfactory results for prolate or oblate ellipsoidal cores with realistic aspect ratios that are $\lesssim$2.

2. *Herschel* observations of B68 and L1689B

As part of the HGBS key project, two fields in the Pipe and Ophiuchus molecular cloud complexes containing B68 and L1689B with areas of $\sim 1.^{\circ}5 \times 1.^{\circ}5$ and $\sim 3.^{\circ}0 \times 3.^{\circ}5$ were observed for an integration time of 2.6 and 10.2 h, respectively. These target fields were mapped[1] in two orthogonal scan directions at a scanning speed of 60″ s^{-1} in parallel mode, acquiring data simultaneously in five bands with the SPIRE (Griffin et al. 2010) and PACS (Poglitsch et al. 2010) bolometer cameras. The data were reduced using HIPE version 7.0. The SPIRE data were processed with modified pipeline scripts. Observations during the turnaround of the telescope were included, and a destriper module with a zero-order polynomial baseline was applied. The default "naïve" mapper was used to produce the final map. For the PACS data, we applied the standard HIPE data reduction pipeline up to level 1 with improved calibration. Further processing of the data, such as subtraction of (thermal and non-thermal) low-frequency noise and map projection was performed with Scanamorphos v11 (Roussel 2012). Note that the Scanamorphos map-maker avoids any high-pass filtering, which is crucial for preserving extended emission.

3. Description of the Abel inversion method

Consider a spherically symmetric core with radial density profile, $\rho(r)$, embedded in a uniform background and isotropic ISRF. Assuming optically thin dust emission, the specific intensity $I_\nu(p)$ of the core when observed at impact parameter, p, may be expressed as

$$I_\nu(p) = 2 \int_p^{+\infty} \rho(r)\, B_\nu\left[T_{\rm d}(r)\right]\, \kappa_\nu \frac{r\,{\rm d}r}{\sqrt{r^2 - p^2}} + I_{\nu,{\rm bg}} + I_{\nu,{\rm N}}, \qquad (1)$$

where $I_{\nu,{\rm bg}}$ and $I_{\nu,{\rm N}}$ represent the background emission and instrumental noise, respectively, $B_\nu[T_{\rm d}(r)]$ is the Planck function for the dust temperature $T_{\rm d}(r)$ at radius r from core center, and κ_ν is the frequency-dependent dust opacity[2], which is assumed here to be uniform throughout the core. Given the symmetry of the problem, we can use the inverse Abel transform (e.g. Bracewell 1986) to obtain the integrand of Eq. (1) at each observed frequency ν:

$$\rho(r)\, B_\nu\left[T_{\rm d}(r)\right]\, \kappa_\nu = -\frac{1}{\pi} \int_r^{+\infty} \frac{{\rm d}I_\nu}{{\rm d}p} \frac{{\rm d}p}{\sqrt{p^2 - r^2}}. \qquad (2)$$

From Eq. (2), we see that the physical parameters of interest, $\rho(r)$ and $T_{\rm d}(r)$, only depend on the first derivatives of the radial intensity profiles. With a pre-defined assumption about the dust opacity law κ_ν, one may thus estimate $T_{\rm d}(r)$ at each radius r by fitting a single-temperature modified blackbody to the SED obtained from evaluating the right-hand side of Eq. (2) at each observed band between 160 μm and 500 μm (see Sect. 3.1 for further details). The density profile, $\rho(r)$, can be derived simultaneously from the normalization of the fit at each radius.

For simplicity, Eq. (1) above neglects the convolution with the telescope beam. However, simulations confirm that beam smearing has little effect in the case of well-resolved cores (see Appendix B). In the case of starless cores, such as B68 and L1689B, with a flat inner density profile inside a radius $R_{\rm flat}$, or angular radius $\theta_{\rm flat}$, we find that the beam effect can be parameterized by the ratio $\theta_{\rm flat}/HPBW$ (where HPBW is the half-power beam width), and that the reconstructed column density profile agrees with the intrinsic profile within 20% (in the absence of noise) for $\theta_{\rm flat}/HPBW \gtrsim 1$ as is the case for B68 and L1689B. More generally, simulations indicate that the reconstructed temperature and column density profiles essentially coincide with the corresponding intrinsic profiles *convolved* to the effective beam resolution (see Appendix B) in the absence of noise. Importantly, our Abel inversion technique does not depend on the subtraction of a flat background level, since the derivative of a constant background[3] does not contribute to the integral of Eq. (2). The reconstruction is, however, quite sensitive to noise fluctuations in the outer parts of the core.

[1] A more detailed description about the observations and data reductions are available on the HGBS archives webpage: http://gouldbelt-herschel.cea.fr/archives. The reduced SPIRE/PACS maps for B68 and L1689B as well as the column density and temperature maps can also be retrieved from the same website.

[2] Note the dust-to-gas fraction of 1% is implicitly included in our definition of the dust opacity (see also Sect. 3.1) so that $\rho(r)$ represents the radial gas density of the object.

[3] If the background is not flat, the input data can be pre-processed by subtracting e.g., a linear plane.

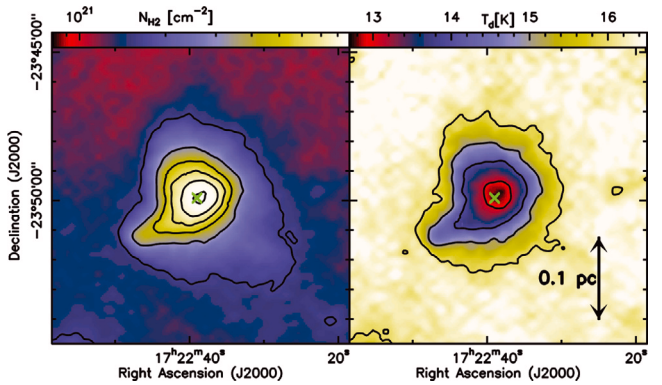

Fig. 1. Column density map (*left*) and LOS dust temperature map (*right*) of B68, which is derived by fitting modified blackbody SEDs to the *Herschel* data between 160 μm and 500 μm on a pixel-by-pixel basis (see Sect. 3.1 for details). The column density contours go from 1.6×10^{21} to 9.6×10^{22} in steps of 1.6×10^{21} in units of H_2 molecules per cm^2 (*left*), and the temperature contours are 16, 15, 14, and 13 K (*right*). The cross symbol shows the center of the core obtained by fitting a 2D-Gaussian to the column density map.

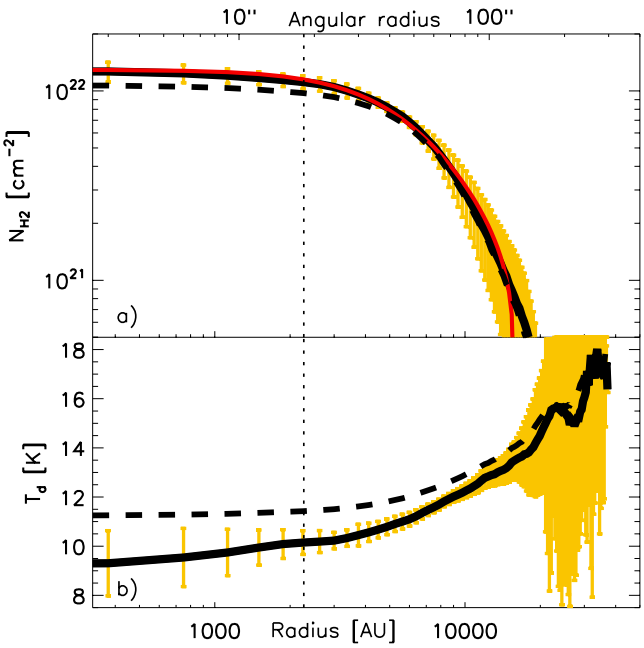

Fig. 2. Column density **a**) and dust temperature **b**) profiles of B68 obtained at 500 μm resolution by applying the Abel inversion method to the circularly averaged intensity profiles observed with *Herschel* between 160 μm and 500 μm. **a**) Comparison between the column density profiles derived from the Abel reconstruction (solid black line) and LOS-averaged SED fitting (thick dashed line). The red curve shows the best-fit Bonnor-Ebert model to the Abel-inverted profile (see Table 2 for parameters). The vertical dotted line represents the half power beam radius of 36.″3/2 (effective 500 μm resolution). **b**) Comparison of the Abel-inverted (solid line) and LOS-averaged SED (dashed curve) temperature profiles. The error bars represent the standard deviation of $N_{H_2}(r)$ and $T_d(r)$ values obtained from independent profile reconstructions along sixteen angular directions.

Table 1. Planck offsets in MJy sr^{-1}.

Target	160 μm	250 μm	350 μm	500 μm
B68	91.2	77.0	41.6	16.6
L1689B	89.3	136.3	64.4	26.6

3.1. SED fitting and profile reconstruction

Column density and corresponding LOS-averaged dust temperature maps are shown in Figs. 1 and 3 for B68 and L1689B, respectively. They were obtained by fitting modified blackbody functions to the *Herschel* SEDs longward of 160 μm on a pixel-by-pixel basis, as seen in earlier HGBS papers (Könyves et al. 2010; see also Hill et al. 2011 for HOBYS). While fitting the SEDs, we weighted each data point by the corresponding calibration errors at SPIRE (∼10%) and PACS (∼15%) wavelengths. Appropriate zero-level offsets were added to each image (see Table 1), which were obtained by correlating the *Herschel* data with the *Planck* and IRAS data of the same fields (see Bernard et al. 2010). The same dust opacity law as in earlier HGBS (see also Motte et al. 2010 for the HOBYS key program) papers is adopted in the present paper (similar to Hildebrand 1983): $\kappa_\lambda = 0.1 \times \left(\frac{\lambda}{300\ \mu\mathrm{m}}\right)^{-\beta}$ cm^2 per g (of gas + dust) with a dust emissivity index of $\beta = 2$. Our dust opacity value at the normalizing wavelength is also close to the Ossenkopf & Henning (1994) opacity model for dust grains with thin ice mantles. A mean molecular weight $\mu_{H_2} = 2.8$ is assumed[4] to express column density in units of H_2 molecules per cm^2. Using our adopted dust opacity law, we find that even the central LOSs for B68 and L1689B with $N_{H_2} \leq 5 \times 10^{22}$ cm^{-2} has small optical depths $\lesssim$0.08 at 160 μm, confirming that the core emission is optically thin longward of 160 μm.

The same assumptions have been adopted for the modified blackbody fits required at each radius by the Abel inversion technique. A single-temperature description of the SEDs is suitable in this case because we are sampling both local density and dust temperature at a given radius r. Prior to the SED fitting, the *Herschel* data are convolved to a common resolution of either 36.″3 (i.e., HPBW resolution of SPIRE at 500 μm) or 24.″9 (i.e., HPBW resolution of SPIRE at 350 μm when the 500 μm data are not used). At each wavelength, a circularly averaged intensity profile about the core center is first derived from the *Herschel* data, and the derivative of this average profile is then numerically evaluated and integrated over the kernel shown in the right-hand side of Eq. (2). The central position of the core is obtained from fitting a 2D-Gaussian model to the column density map (see the cross symbols in Figs. 1 and 3 for B68 and L1689B, respectively). The integration is performed up to an outer radius corresponding to ∼2–2.5 times the *FWHM diameter* of the core as estimated from the 2D-Gaussian fit to the column density map. In practice, the integral on the right-hand side of Eq. (2) converges rapidly and does not depend much on the precise value of the integration outer radius as long as it encompasses the entire core – see Appendix A and Fig. A.1.

3.2. Assessment of uncertainties

The errors bars on the reconstructed profiles at each radius can be estimated from the standard deviations of the density and temperature profiles obtained by repeating the Abel reconstruction along different angular directions around the source (i.e., averaging the data separately over a series of angular sectors instead of circularly averaging the data). In the case of the reconstructed profiles of B68 and L1689B as shown in Figs. 2 and 4,

[4] Note that this differs from the first HGBS papers (e.g. André et al. 2010; Könyves et al. 2010; Arzoumanian et al. 2011), where $\mu = 2.33$ was assumed and column density was expressed in units of mean free particles per cm^2.

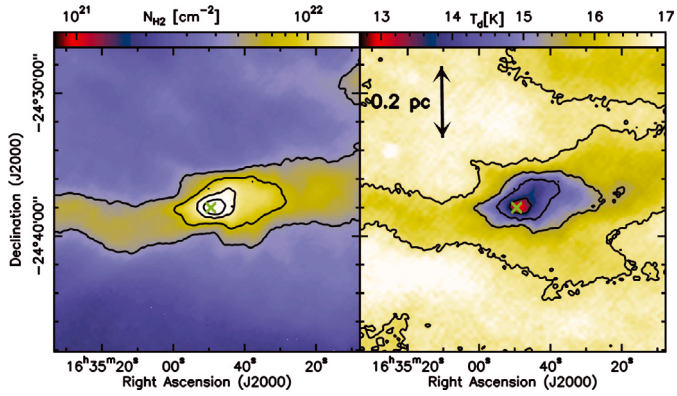

Fig. 3. Same as Fig. 1 but for L1689B. The column density contours are 6×10^{21}, 1×10^{22}, 1.4×10^{22}, 1.8×10^{22}, and 2.6×10^{22} H_2 cm^{-2} (*left*), and the temperature contours are 16.5, 15.5, 14.5, and 13.5 K (*right*). The column density image shows that L1689B is embedded inside a filamentary structure.

sixteen equally-spaced angular sectors were used to derive the error bars. The errors we report on the best estimates of the (column) density and temperature at core center correspond to the standard error in the mean, $\sigma/\sqrt{n}$, where n is the number of independently measured sectors.

The uncertainty in the normalization of the dust opacity law directly affects the column density estimates but not the temperature estimates, whereas the uncertainty in the emissivity index β influences both the dust temperature and the column density estimates in an anti-correlated fashion. When β is varied from 2 to 1.5, for instance, the dust temperature increases by ∼10% and the column density decreases by ∼40%. The uncertainty in the central position of the core also introduces errors on the derived parameters. To assess the magnitude of this effect in the case of B68, we varied the central position within a radius of 6″ and found that the resulting central dust temperature and central column density had standard deviations of ±0.3 K and $\pm 0.04 \times 10^{22}$ cm^{-2}, respectively. Additionally, departures from spherical symmetry due to asymmetries in the density distribution (cf. L1689B in Fig. 3) or an anisotropic background radiation field (cf. Nielbock et al. 2012) may break the symmetry of the quantity $\rho(r)B_\nu(T(r))$ in Eqs. (1) and (2), introducing additional errors. In principle the latter are included in the error bars estimated from the fluctuations of the radial profiles reconstructed along various angular directions. Moreover, we show in Appendix B that cores with moderate departures from spherical symmetry (such as prolate or oblate ellipsoidal cores with aspect ratios ≲2) can be reconstructed with reasonable accuracy.

For both B68 and L1689B, the net measurement errors in the derived central T_d and N_{H_2} values are estimated to be ±0.5 K and $\pm 0.1 \times 10^{22}$ cm^{-2}, respectively, excluding the systematic uncertainties associated with our assumptions on the dust opacity and the calibration errors. In Appendix B.1 we show that the calibration errors lead to an additional uncertainty of ∼12% on column density and ∼5% on temperature estimates.

4. Detailed results for B68 and L1689B

4.1. B68 core

B68 is a well studied isolated bok globule in the Pipe nebula cloud complex (e.g. Alves et al. 2001; Nielbock et al. 2012). We adopt a distance of 125 pc (de Geus et al. 1989) for the present study. Figure 2 shows the reconstructed column density and temperature profiles obtained from our *Herschel* observations of B68 with the Abel inversion method described as in Sect. 3.

In Fig. 2b, the Abel-inverted radial dust temperature profile (solid curve) is compared with the LOS-averaged SED temperature profile (dashed curve). While both temperature profiles exhibit similar features with a broad minimum around the core center, a positive gradient outside the flat inner plateau of the column density profile, and similar values ($T_d \sim 16.5 \pm 2$ K) at large radii, the minimum Abel-reconstructed temperature at core center is ∼2 K lower than the minimum SED temperature observed through the central LOS. Accordingly, the central column density derived with the Abel inversion method ($1.3 \pm 0.1 \times 10^{22}$ cm^{-2}) is 30% higher than the LOS-averaged column density of $\sim 1.0 \times 10^{22}$ cm^{-2} that is derived from standard SED fitting for the central LOS. The difference between the Abel-reconstructed and the LOS-averaged column density becomes negligible in the outer parts of the core. This is indicative of stronger temperature variations along the central LOS compared to the outer LOSs.

Recently, Nielbock et al. (2012) constrained the dust temperature and volume density profiles of B68 using an iterative approach based on 3D radiative transfer modeling of multiwavelength dust continuum data. This included *Herschel* observations that were obtained as a part of the EPoS (Launhardt et al. 2013) key project. They employed a 3-dimensional grid of Plummer-like (Plummer 1911) density profiles and obtained initial guesses of the parameters from LOS-averaged SED fits. Altogether their model was tuned with eight free parameters, yielding a central dust temperature of $T_d = 8.2^{+2.1}_{-0.7}$ K. The primary reason for the dispersion in the central dust temperature in Nielbock et al. (2012) is the uncertainty of a factor of ∼2 on the dust opacity in the infrared regime. Although we obtain a higher central dust temperature, $T_d = 9.3 \pm 0.5$ K, with our Abel-inversion method, our results agree with the Nielbock et al. analysis within the range of the quoted uncertainties.

Based on extinction measurements (Alves et al. 2001), the column density profile of B68 closely resembles that of a Bonnor-Ebert (BE; e.g., Bonnor 1956) isothermal sphere with a flattened inner region. The overplotted red curve in Fig. 2 shows the best-fit BE model to the reconstructed column density profile. The best-fit BE parameters along with the physical properties that follow directly from the fit such as the radius of the flat inner plateau, $R_{flat} \equiv 2\,c_s/\sqrt{4\pi G \rho_c}$, the density contrast, ρ_c/ρ_s, and the external pressure, P_{ext}, are summarized in Table 2. They are consistent with the BE parameters found by Alves et al. (2001).

The N_{H_2} column density profile obtained by integrating the Abel-inverted volume density profile is shown in Fig. 2. This can be directly compared with the near-infrared extinction results Alves et al. (2001) because extinction traces material independently of temperature. For this comparison, we adopted a standard conversion factor, N_{H_2}/A_V of 9.4×10^{20} cm^{-2} mag^{-1} (Bohlin et al. 1978), to translate column density to equivalent visual extinction A_V at low column densities (i.e., $N_{H_2} \lesssim 6 \times 10^{21}$ cm^{-2}). For higher column densities, we used the conversion $N_{H_2}/A_V = 6.9 \times 10^{20}$ cm^{-2} mag^{-1} given by Draine (2003) and later adopted by Evans et al. (2009), which is consistent with an extinction curve with a total-to-selective extinction, $R_V \equiv A_V/E(B-V) = 5.5$ that is appropriate in higher density regions.

Using the Bohlin conversion factor, we obtain an A_V of 3.2 mag at a radius of 10^4 AU, which agrees within ∼60% with the value of 5 mag reported by Alves et al. (2001) at the

Table 2. Best-fit parameters of Bonnor-Ebert core models for B68 and L1689B.

Source profile	ξ_{max}	ρ_c/ρ_s [a]	c_s [b] (km s^{-1})	P_{ext} (K cm^{-3}) $\times 10^4$	R_{flat} [c] (AU) $\times 10^3$	R_{out} (AU) $\times 10^4$	n_c (cm^{-3}) $\times 10^4$
B68	7.0 ± 0.1	17	0.17	3.9	4.4	1.5	8.3
L1689B-C	16.6 ± 0.7	145	0.27	2.9	4.5	3.7	20
L1689B-NS	13.5 ± 0.3	88	0.24	3.2	4.4	2.9	17
L1689B-EW	16.2 ± 1.7	137	0.26	2.2	4.7	3.8	16.5

Notes. [(a)] ρ_c and ρ_s denote central density and density at the outer surface of the BE sphere, respectively. [(b)] Isothermal sound speed. [(c)] Flat inner radius, defined as $R_{flat} \equiv 2\,c_s/\sqrt{4\pi G\rho_c}$.

same radius. Furthermore, if we correct our estimate for the weak empirical trend between submillimeter dust opacity and column density, $\kappa_\lambda \propto {N_{H_2}}^{0.28}$, as inferred by Roy et al. (2013) in the regime of $1 \lesssim A_V \lesssim 10$ and interpreted as evidence of dust grain evolution, then we find a corrected column density $N_{H_2}^{corr} \approx 5 \times 10^{21}$ cm^{-2}, which is equivalent to a corrected $A_V^{corr} = 5.3$ mag. This is in excellent (10%) agreement with Alves et al. (2001) at 10^4 AU.

Using the Draine conversion factor, we derive an A_V of 19 ± 2 mag through the center of the B68 core as compared to the A_V of 30 mag obtained from extinction by Alves et al. (2001), corresponding to a 60% agreement. However, the effective angular resolution of the Alves et al. extinction map was about ∼10″, approximately four times higher than the beam resolution (36.″3) of SPIRE at 500 μm. For better comparison, we performed a similar Abel reconstruction analysis at the beam resolution (24.″9) of the SPIRE 350 μm observations, ignoring the 500 μm data. In this case, the central Abel-reconstructed column density corresponds to $A_V = 20 \pm 2$ mag, which agrees within 50% with the results of Alves et al. (2001). (The central dust temperature derived at 350 μm resolution coincides within the uncertainties with the 500 μm resolution estimate.)

Likewise, the total mass of 1.6 ± 0.07 $M_\odot$, which is derived by integrating the Abel-reconstructed density profile of B68 within the outer radius of 1.4×10^4 AU, agrees within 30% with the mass of 2.1 $M_\odot$ as obtained by Alves et al. (2001) from the extinction data. For comparison, the mass derived from fitting a modified blackbody to the integrated flux densities is 1.4 ± 0.05 $M_\odot$. The latter does not account for temperature variations along the LOS and thus slightly underestimates the intrinsic total mass of the core. For a moderate density core such as B68, however, we stress that the global SED temperature (12.5±0.1 K here) is close to the mass-averaged dust temperature and the SED mass agrees within ∼15% of the Abel-reconstructed mass.

Using the above results on the density and temperature structure, we can check the energy balance of the B68 core. Assuming optically thin submillimeter emission, a total output luminosity of 0.35 ± 0.04 $L_\odot$ is obtained by integrating the quantity $4\pi \int \rho(r) B_\nu[T_d(r)]\kappa_\nu d\nu$ over the volume of the core. A very similar output luminosity (0.41 ± 0.05 $L_\odot$) is estimated by integrating the observed SED over wavelengths. These output estimates should be compared to the input luminosity of ∼0.40 $L_\odot$ provided to the core by the local ISRF (Mathis et al. 1983; with $G_0 \sim 1$), which are calculated from the total ISRF flux density that is absorbed[5] by a spherical object with the same density profile and outer radius as B68 using Eq. (4) of Lehtinen et al. (1998). Note that the three luminosity values above agree with one another.

4.2. L1689B

Compared to B68, L1689B is a slightly denser and more centrally condensed core (e.g. André et al. 1996; Bacmann et al. 2000) located in the Ophiuchus complex at a distance of ∼140 pc. The *Herschel* images reveal that it is embedded within a larger-scale filamentary structure (see Fig. 3). Given the elongated morphology that is observed in the plane of the sky and the mean apparent aspect ratio ∼1.3 of the core, the hypothesis of spherical symmetry underlying Eq. (1) is not strictly verified.

To assess the validity of our Abel-inversion scheme in this case, we therefore performed test reconstructions for prolate and oblate ellipsoidal model cores with similar aspect ratios. These tests suggest that small departures from spherical symmetry have little impact on the reconstruction results (see Appendix B).

The upper panel of Fig. 4 shows the results of three distinct reconstructions of the column density profile of L1689B, as obtained by applying the Abel inversion method to a) the circularly averaged intensity profiles (thick solid curve); b) the intensity profiles observed in sectors oriented east-west (EW), i.e., approximately along the apparent major axis of the core (blue dash-dotted curve); and c) the intensity profiles observed in sectors oriented north-south (NS), i.e., approximately along the apparent minor axis of the core (green dash-dotted curve). While the three column density profiles agree with each other within the central plateau region, the EW profile lies 30% above the NS profile at large radii $\gtrsim 10^4$ AU, and the circularly averaged profile is intermediate between the other two. For reference and comparison with B68, a BE model was fitted to each of the three column density profiles and the results of these fits are given in Table 2. (For the sake of clarity, only the model fit to the circularly averaged intensity profiles is shown in Fig. 4, as a red solid curve.) All three fits yield a consistent value for the radius of the flat inner plateau, $R_{flat} \sim 4500 \pm 100$ AU (corresponding to ∼32″). The average reconstructed column density within R_{flat} is $3.5 \pm 0.1 \times 10^{22}$ cm^{-2}, which agrees well (∼30%) with the H_2 column density that is averaged over the flat inner part of the core of $4.5–4.7 \times 10^{22}$ cm^{-2}. This value was found by Bacmann et al. (2000) based on their ISOCAM mid-infrared absorption study (see their Table 2).

Our best estimate of the total core mass obtained from Abel reconstructing is 11 ± 2 $M_\odot$. The tests we performed for ellipsoidal synthetic cores (cf. Appendix B) indicate that the relative error in this mass introduced by the departure from spherical

[5] The ISRF energy is mostly absorbed at short wavelengths (0.095 μm to 100 μm). In calculating the absorbed energy we adopted the dust absorption model of Draine (2003) with $R_V = 3.1$.

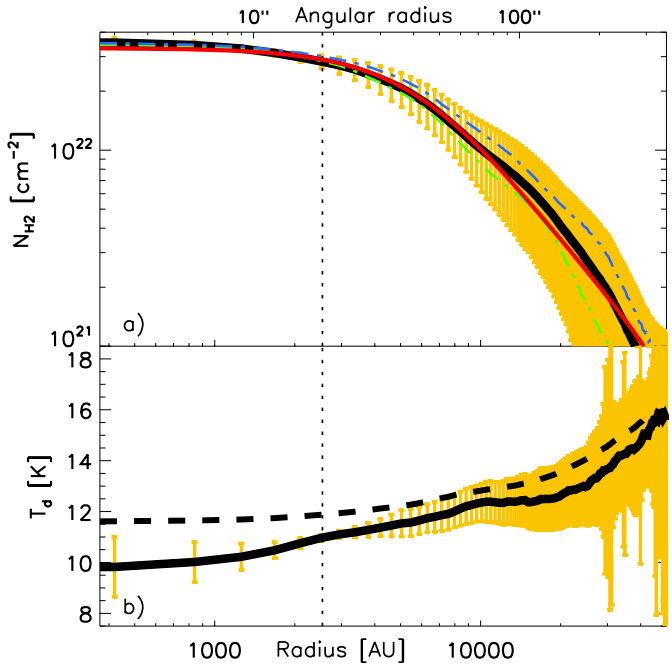

Fig. 4. a) Column density profile of L1689B obtained at 500 μm resolution by applying the Abel reconstruction method to the circularly averaged intensity profiles between 160 μm and 500 μm (solid black curve). The dash-dotted blue and green profiles show the column density profiles obtained from reconstructing the intensity profiles observed along EW and NS sectors, respectively. The overplotted solid red line shows the best-fit Bonnor-Ebert model (see Table 2 for parameters). The vertical dotted line is same as in Fig. 2. **b)** Reconstructed dust temperature profile of L1689B (solid curve) compared with the LOS-averaged temperature profile derived from simple SED fitting (thick dashed curve).

symmetry is less than 4% for an intrinsic aspect ratio of ~1.3. Our mass estimate is in excellent agreement with the total mass reported by Bacmann et al. (2000). The SED mass derived from fitting a modified blackbody to the integrated flux densities is 7.8 ± 0.2 $M_\odot$, which is about 30% lower than our best mass estimate. The corresponding global SED temperature of the core is 12.5 ± 0.2 K.

The central dust temperature obtained for L1689B using the Abel transform technique is 9.8 ± 0.5 K (see lower panel of Fig. 4). This value is higher than the very low central dust temperature of 7.5 K advocated by Evans et al. (2001) which is based on radiative transfer calculations if a standard ISRF (G_0 = 1) is assumed. At least part of this discrepancy can be explained by the fact that the effective external radiation field for L1689B is about one order of magnitude stronger than the standard ISRF, due to the presence of early-type stars in the immediate vicinity of the Ophiuchus cloud (cf. Liseau et al. 1999).

5. Conclusions

The results of B68 and L1689B discussed in Sect. 4, along with the tests on model cores presented in Appendix B, demonstrate that the Abel transform technique can successfully produce meaningful radial density and dust temperature profiles for spatially resolved prestellar cores. The most rewarding result is the reconstruction of a radial dust temperature profile that is directly from *Herschel* dust continuum imaging data and independent of any radiative transfer model. The Abel inversion technique (Sect. 3) is very general: it is insensitive to background subtraction to first order and can perform equally well for externally-heated (isotropically) starless cores or internally-heated protostellar cores. While the technique assumes spherically symmetric cores in principle, tests performed on ellipsoidal cores suggest that satisfactory results are obtained even when the hypothesis of spherical symmetry is not strictly valid (such as in the L1689B case – cf. Fig. 3). A similar Abel-transform scheme may also be employed to reconstruct the intrinsic beam-averaged density and temperature profiles of (approximately) cylindrically symmetric filaments from the observed radial intensity profiles averaged along the filament main axes.

For both B68 and L1689B, we find a characteristic dip in the dust temperature profile with minimum beam-averaged values of 9.3 ± 0.5 K and 9.8 ± 0.5 K at core center, respectively. The temperature profile smoothly merges with the background cloud temperature at the outer core radii.

The Abel transform technique yields central beam-averaged H_2 densities of $7.5 \pm 0.5 \times 10^4$ cm^{-3} and $2.0 \pm 0.1 \times 10^5$ cm^{-3} for B68 and L1689B, respectively, which correspond to central column densities of $1.3 \pm 0.1 \times 10^{22}$ cm^{-2} and $3.6 \pm 0.1 \times 10^{22}$ cm^{-2} after integration of the reconstructed volume density profiles along the LOS. These central column density estimates are approximately 15% larger than the values obtained from direct SED fitting. Comparison of our results with the independent near-IR extinction measurement of the B68 column density profile by Alves et al. (2001) suggests that the dust opacity law adopted by the HGBS consortium, with $\kappa_{300\,\mu m}$ = 0.1 cm^2 per g (of gas + dust) at λ = 300 μm and β = 2, is more accurate than (and possibly overestimated by) 50% in the 160–500 μm range. This value is for sources of (column) densities that are comparable to B68 and L1689B. Our adopted opacity value is within ~20% of the value[6] obtained by Suutarinen et al. (2013) for the dust inside a core of similar column density to the ones considered here. Assuming that the weak trend between submillimeter dust opacity and column density ($\kappa_\lambda \propto {N_{H_2}}^{0.28}$) found by Roy et al. (2013) at $A_V \lesssim 10$ also holds at higher A_V, we argue that the HGBS dust opacity law may remain valid to within 50% accuracy in the whole range of H_2 column densities between ~3×10^{21} cm^{-2} and ~10^{23} cm^{-2}.

Since the Abel transformation technique can help us correct the effect of LOS temperature variations on the derivation of total masses, we conclude that the *Herschel* data of the HGBS project holds the promise of delivering core masses to accuracy more than factor of 1.5 to 2, at least for spatially-resolved cores.

Acknowledgements. This work has benefited from the support of the CNES and the European Research Council under the European Union's Seventh Framework Programme (FP7/2007-2013 – ERC Grant Agreement no. 291294). P.P. acknowledges funding by the Fundação para a Ciência e a Tecnologia (Portugal). SPIRE has been developed by a consortium of institutes led by Cardiff Univ. (UK) and including Univ. Lethbridge (Canada); NAOC (China); CEA, LAM (France); IFSI, Univ. Padua (Italy); IAC (Spain); Stockholm Observatory (Sweden); Imperial College London, RAL, UCL-MSSL, UKATC, Univ. Sussex (UK); Caltech, JPL, NHSC, Univ. Colorado (USA). This development has been supported by national funding agencies: CSA (Canada); NAOC (China); CEA, CNES, CNRS (France); ASI (Italy); MCINN (Spain); SNSB (Sweden); STFC (UK); and NASA (USA). PACS has been developed by a consortium of institutes led by MPE (Germany) and including UVIE (Austria); KUL, CSL, IMEC (Belgium); CEA, OAMP (France); MPIA (Germany); IFSI, OAP/AOT, OAA/CAISMI, LENS, SISSA (Italy); IAC (Spain). This development has been supported by the funding agencies BMVIT (Austria), ESA-PRODEX (Belgium), CEA/CNES (France), DLR (Germany), ASI (Italy), and CICT/MCT (Spain).

[6] Suutarinen et al. 2013 quote $\kappa_{250\,\mu m}$ = 0.08 cm^2 g^{-1} with β = 2 and argue that this value is underestimated by 40% inside the core due to temperature variations along the LOS.

References

Alves, J. F., Lada, C. J., & Lada, E. A. 2001, Nature, 409, 159
André, P., Ward-Thompson, D., & Motte, F. 1996, A&A, 314, 625
André, P., Bouwman, J., Belloche, A., & Hennebelle, P. 2003, in Proc. SFChem 2002: Chemistry as a Diagnostic of Star Formation, eds. C. L. Curry, & M. Fich (Ottawa: NRC Press), 127
André, P., Men'shchikov, A., Bontemps, S., et al. 2010, A&A, 518, L102
Arzoumanian, D., André, P., Didelon, P., et al. 2011, A&A, 529, L6
Bacmann, A., André, P., Puget, J.-L., et al. 2000, A&A, 361, 555
Bernard, J.-P., Paradis, D., Marshall, D. J., et al. 2010, A&A, 518, L88
Bohlin, R. C., Savage, B. D., & Drake, J. F. 1978, ApJ, 224, 132
Bonnor, W. B. 1956, MNRAS, 116, 351
Bouwman, J., Meeus, G., de Koter, A., et al. 2001, A&A, 375, 950
Bracewell, R. N. 1986, The Fourier Transform and its applications, 2nd edn. (New York: McGraw-Hill)
de Geus, E. J., de Zeeuw, P. T., & Lub, J. 1989, A&A, 216, 44
Draine, B. T. 2003, ARA&A, 41, 241
Evans, II, N. J., Rawlings, J. M. C., Shirley, Y. L., & Mundy, L. G. 2001, ApJ, 557, 193
Evans, II, N. J., Dunham, M. M., Jørgensen, J. K., et al. 2009, ApJS, 181, 321
Griffin, M. J., Abergel, A., Abreu, A., et al. 2010, A&A, 518, L3
Hildebrand, R. H. 1983, QJRAS, 24, 267
Hill, T., Motte, F., Didelon, P., et al. 2011, A&A, 533, A94
Kirk, J. M., Ward-Thompson, D., & André, P. 2005, MNRAS, 360, 1506
Könyves, V., André, P., Men'shchikov, A., et al. 2010, A&A, 518, L106
Launhardt, R., Stutz, A. M., Schmiedeke, A., et al. 2013, A&A, 551, A98
Lehtinen, K., Lemke, D., Mattila, K., & Haikala, L. K. 1998, A&A, 333, 702
Liseau, R., White, G. J., Larsson, B., et al. 1999, A&A, 344, 342
Malinen, J., Juvela, M., Collins, D. C., Lunttila, T., & Padoan, P. 2011, A&A, 530, A101
Marsh, K. A., Griffin, M. J., André, P., et al. 2014, MNRAS, submitted [arXiv:1401.7871]
Mathis, J. S., Mezger, P. G., & Panagia, N. 1983, A&A, 128, 212
Men'shchikov, A., André, P., Didelon, P., et al. 2012, A&A, 542, A81
Motte, F., Zavagno, A., Bontemps, S., et al. 2010, A&A, 518, L77
Nielbock, M., Launhardt, R., Steinacker, J., et al. 2012, A&A, 547, A11
Ossenkopf, V., & Henning, T. 1994, A&A, 291, 943
Pilbratt, G. L., Riedinger, J. R., Passvogel, T., et al. 2010, A&A, 518, L1
Plummer, H. C. 1911, MNRAS, 71, 460
Poglitsch, A., Waelkens, C., Geis, N., et al. 2010, A&A, 518, L2
Roussel, H. 2012, PASP, 125, 1126
Roy, A., Martin, P. G., Polychroni, D., et al. 2013, ApJ, 763, 55
Stamatellos, D., Whitworth, A. P., & Ward-Thompson, D. 2007, MNRAS, 379, 1390
Suutarinen, A., Haikala, L. K., Harju, J., et al. 2013, A&A, 555, A140
Ward-Thompson, D., André, P., & Kirk, J. M. 2002, MNRAS, 329, 257
Ysard, N., Juvela, M., Demyk, K., et al. 2012, A&A, 542, A21

Pages 8 to 10 are available in the electronic edition of the journal at http://www.aanda.org

Appendix A: Surface brightness profiles and the outer radius of B68

The top panel of Fig. A.1 shows the circularly averaged intensity profiles of the B68 core at SPIRE and PACS wavelengths, which were used to construct the column density and temperature profiles shown in Fig. 2. The bottom panel of Fig. A.1 shows the logarithmic slope of the column density profile (black line), which is defined as $s \equiv \mathrm{d}\ln N_{\mathrm{H_2}}/\mathrm{d}\ln r$ (dimensionless), as a function of radius. The measured logarithmic slope is $s = 0$ near the core center due to flat inner density profile and the finite resolution of the observations. The logarithmic slope profile reaches a minimum value $s_{\mathrm{min}} \sim -1.5$ at $r \sim 10^4$ AU and goes back to $s \sim 0$ at the outer boundary, where the core merges with a slowly-varying background. For comparison, a spherical core with outer density profile $\rho \propto r^{-2}$ would have $s = -1$ at large radii. In the same plot, we show the logarithmic slope of the 500 μm surface brightness profile (blue line), which has a shallower slope due to the additional effect of the positive outward temperature gradient. Inspection of the intensity and slope profiles shown in Fig. A.1 allows us to select an appropriate upper integration radius in the right-hand side of Eq. (2) when the density and temperature structure of B68 (see Sect. 3) are reconstructed. Since $\frac{\mathrm{d}I_\nu}{\mathrm{d}p} = s \times \frac{I_\nu}{p} \approx 0$ beyond a radius ~25 000 AU, larger radii do not contribute to the integral of Eq. (2). In practice, we adopt an upper integration radius $R_{\mathrm{up}} = 37\,500$ AU for B68, as shown by the dashed vertical line in Fig. A.1. The reconstruction results, however, are insensitive to the precise choice of R_{up} as long as $R_{\mathrm{up}} \gtrsim 25\,000$ AU. The adjacent dot-dashed vertical line shows the effective radius of ~27 000 AU (or ~200″), as derived by the *getsources* source-finding algorithm for the "footprint" of B68. The *getsources* algorithm (Men'shchikov et al. 2012) is the source extraction method used by the HGBS consortium to produce the first-generation catalogs of dense cores found by *Herschel* in the regions covered by the HGBS survey. The footprint of a core corresponds to the area just outside, of which *getsources* estimates the local background emission and over which it integrates the background-subtracted emission to derive the total flux densities of the core. In the case of B68, the results automatically derived by *getsources* are in excellent agreement with those obtained through a detailed radial profile analysis (cf. Fig. A.1).

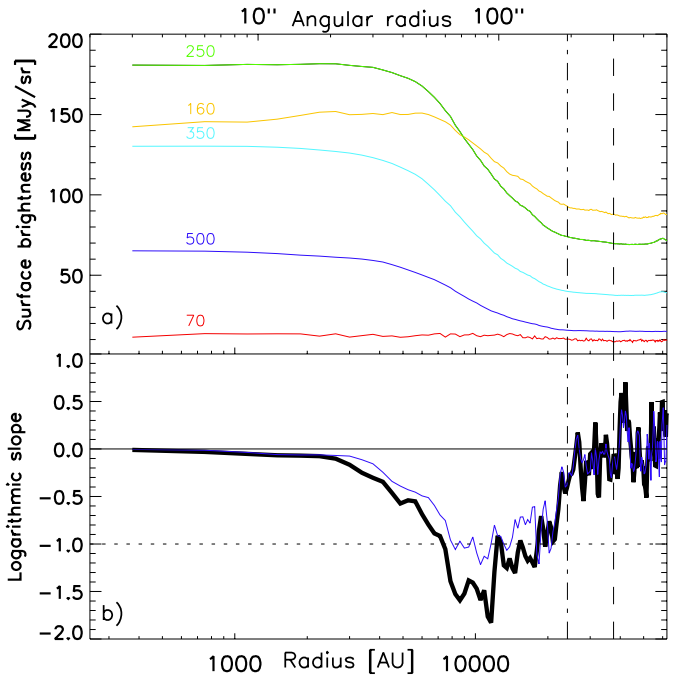

Fig. A.1. **a)** Circularly averaged radial surface brightness profiles of B68 at 70, 160, 250, 350, 500 μm derived from *Herschel*/SPIRE and PACS data (after adding Planck offsets). **b)** Logarithmic slopes of the circularly averaged column density profile (solid black curve) and 500 μm intensity profile (solid blue curve) of B68 as a function of radius. The horizontal dotted line is the logarithmic slope $s = -1$ expected for the column density profile of a core with a $\rho \propto r^{-2}$ density profile. The vertical dashed line marks the integration upper bound adopted when integrating the right-hand side of Eq. (2) to perform the Abel reconstruction of the density and temperature profiles (see Sect. 3). The vertical dot-dashed line shows the radius of the footprint automatically derived for B68 by the *getsources* source-finding algorithm.

Appendix B: Tests of the Abel inversion method using simple models

B.1. Spherically symmetric core model

To test the performance level of our Abel inversion scheme and quantify the robustness of the reconstruction, we applied the algorithm as described in Sect. 3 to synthetic images corresponding to model starless cores of known density and temperature distributions. First, we considered a spherically-symmetric core model with a Plummer-type density distribution for $r \leq R_{\mathrm{out}}$,

$$\rho(r) = \frac{\rho_{\mathrm{c}}}{1 + (r/R_{\mathrm{flat}})^2}, \tag{B.1}$$

which is parameterized by physical parameters that are approximately similar to the derived properties of B68 (see Sect. 4.1): central H_2 number density $n_{\mathrm{c}} \equiv \rho_{\mathrm{c}}/\mu_{\mathrm{H_2}} m_{\mathrm{H}} = 8 \times 10^4$ cm^{-3}, flat inner radius $R_{\mathrm{flat}} = 5 \times 10^3$ AU, and outer radius $R_{\mathrm{out}} = 1.5 \times 10^4$ AU. The surface density profile of such a model core has an analytical form of

$$\Sigma(p) = \frac{2\rho_{\mathrm{c}} R_{\mathrm{flat}}}{\left(1 + p^2/R_{\mathrm{flat}}^2\right)^{1/2}} \times \tan^{-1}\left\{\frac{(R_{\mathrm{out}}^2 - p^2)^{1/2}}{(R_{\mathrm{flat}}^2 + p^2)^{1/2}}\right\}, \tag{B.2}$$

where p represents the impact parameter from core center in the plane of the sky and $N_{\mathrm{H_2}}(p) = \Sigma(p)/\mu_{\mathrm{H_2}} m_{\mathrm{H}}$ is the H_2 column density profile. The intrinsic density profile of the model is shown as a black solid curve in Fig. B.1a and the corresponding column density profile as a black solid curve in Fig. B.1b. The synthetic dust temperature profile is shown as a black solid curve in Fig. B.1c and was obtained for a solar-neighborhood ISRF ($G_0 = 1$) using an analytic approximation formula that reproduces a grid of spherically symmetric models performed with the dust radiative transfer code MODUST (Bouwman et al., in prep.; see Bouwman et al. 2001; and André et al. 2003).

A set of synthetic emission maps was created by line-of-sight integration of this model core at all *Herschel* wavelengths, assuming optically thin dust emission (see Eq. (1)) and the same dust opacity law as given in Sect. 3.1. The density and temperature profiles of the model core were then reconstructed as described in Sect. 3 from the circularly averaged radial intensity profiles of the model emission. The cross symbols overlaid on the model density, column density, and temperature profiles in Fig. B.1a–c show the Abel-reconstructed profiles that would be obtained with "infinite" angular resolution (and in the absence of

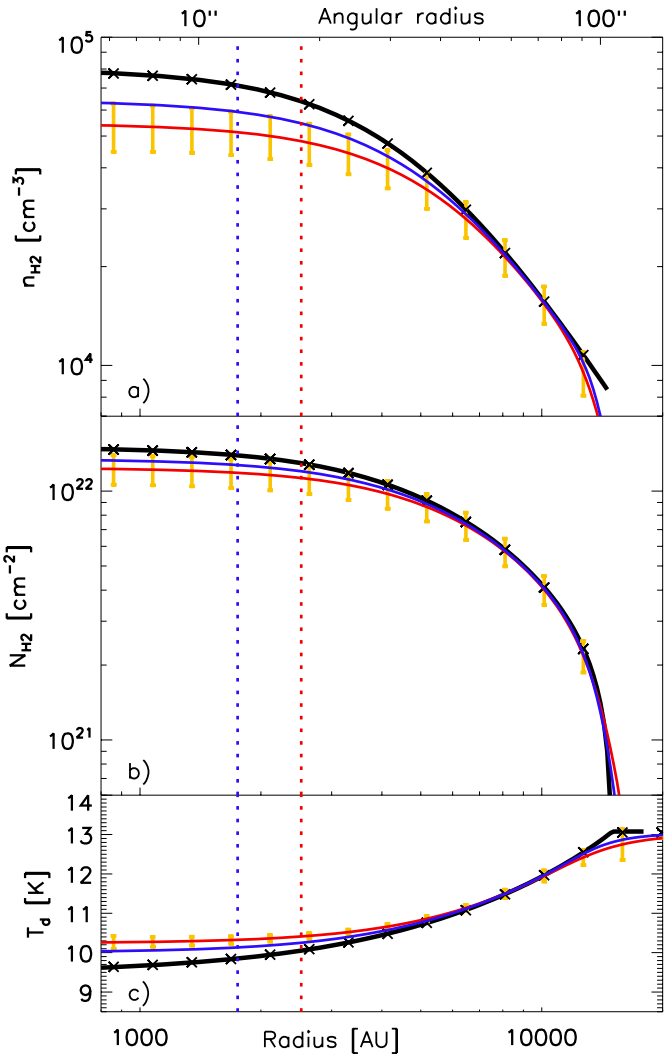

Fig. B.1. Comparison between intrinsic (black curves) and reconstructed (red and blue curves) volume density **a)**, column density **b)**, and dust temperature **c)** profiles for a spherically symmetric core model with a Plummer-like density distribution (see Eq. (B.1) and text for model parameters). The cross symbols show the results obtained by applying the Abel reconstruction scheme on the synthetic 160–500 μm intensity profiles with "infinite" resolution. The red and blue curves show the reconstruction results obtained from synthetic emission maps smoothed to HPBW resolutions of 36.″3 and 24.″9, respectively, corresponding to the resolutions of *Herschel* 500 μm and 350 μm observations. Note the good agreement between the reconstructed profiles and the intrinsic profiles beyond the the half power beam radius of 36.″3/2 (500 μm resolution) or 24.″9/2 (350 μm resolution), as marked by the red and blue vertical dotted lines, respectively. The error bars in each panel show the 1σ uncertainties due to random noise and calibration errors.

noise). It can be seen in Fig. B.1 that, the reconstruction is perfect in this case, demonstrating the validity of our Abel-inversion code. The overplotted red curves in Fig. B.1a–c show the reconstructed volume density, column density, and temperature profiles that result from the Abel-inversion method after convolution of the model images to a common resolution of 36.″3. This corresponds to the *Herschel* resolution at 500 μm. Likewise, the overplotted blue curves in Fig. B.1a–c show the results obtained at a resolution of 24.″9 using the synthetic data convolved to the *Herschel* resolution at 350 μm and ignoring the 500 μm data. It can be seen that the profiles reconstructed at the *Herschel* resolution remain in excellent (1%) agreement with the intrinsic profiles in the outer part of the core. Although the reconstruction becomes somewhat inaccurate below the *Herschel* resolution limit (marked by vertical dotted lines in Fig. B.1), the reconstructed column density and temperature profiles still agree with the corresponding intrinsic profiles to within 20% and 9%, respectively, at 500 μm resolution. The accuracy of the results at small radii improves to 11% and 5% when the reconstruction is performed at 350 μm resolution. (Although in the presence of noise with real data, the statistical measurement uncertainties are somewhat larger at 350 μm resolution.) At both resolutions, the Abel-reconstructed temperature and column density profiles coincide within 1% with the corresponding intrinsic profiles that are *convolved* with the effective beam resolution. The reconstructed central temperature and column density thus provide excellent estimates of the beam-averaged central temperature and column density in the model. The total mass that is estimated by integrating the reconstructed column density profile agrees with the model mass more accurate than 0.1% even at 500 μm resolution.

We also assessed the contribution of background fluctuations and calibration errors to the uncertainties in the derived parameters ($N_{\rm H_2}$and $T_{\rm d}$). To do so, we considered 500 realizations of synthetic skies, which included a random Gaussian noise component[7], σ_ν, and a random multiplicative calibration factor, $(1 + g)$:

$$I_\nu^{\rm sim}(x, y) = [I_\nu^{\rm model}(x, y) + \sigma_\nu](1 + g), \tag{B.3}$$

where g is a Gaussian random number with a mean zero and standard deviation of 10% and 15% at SPIRE and PACS wavelengths, respectively. (We assumed 100% correlated calibration errors at SPIRE wavelengths and an independent calibration error in the PACS 160 μm band.) The net uncertainties in $n_{\rm H_2}$, $N_{\rm H_2}$, and $T_{\rm d}$ were estimated to be 15%, 12%, and 5%, respectively. The resulting 1σ errors in the derived parameters are displayed in Fig. B.1.

B.2. Ellipsoidal core model

As real cores, such as L1689B, are often elongated and thus not strictly spherically symmetric (see Sect. 4.2), we also tested the reliability of our Abel inversion scheme using a simple non-spherical model with an ellipsoidal Plummer-like density distribution for $r \le R_{\rm out}$ and $z \le Z_{\rm out}$ with cylindrical symmetry about the z axis (assumed to lie in the plane of the sky):

$$\rho(r, z) = \frac{\rho_c}{1 + (r/R_{\rm flat})^2 + (z/Z_{\rm flat})^2}, \tag{B.4}$$

where $R_{\rm flat}$ and $Z_{\rm flat}$ are the radii of the flat inner core region perpendicular and parallel to the z axis of symmetry (see Fig. B.2a), respectively. We considered both the prolate ($Z_{\rm flat} > R_{\rm flat}$) and the oblate ($Z_{\rm flat} < R_{\rm flat}$) configuration but are primarily describing the prolate case here, as it is more likely for cores embedded within filaments such as L1689B (see Fig. 3). The synthetic temperature distribution was also assumed to be cylindrically symmetric about the z axis and was constructed using the same grid of MODUST radiative transfer models as in Appendix B.1. The synthetic temperature profiles along both the z axis and the radial (r) direction are shown in Fig. B.2. For direct comparison

[7] The level of noise fluctuations (σ_ν) was chosen so that the peak signal-to-noise $I_\nu^{\rm peak}/\sigma_\nu$ value at each wavelength was consistent with the corresponding B68 surface brightness image.

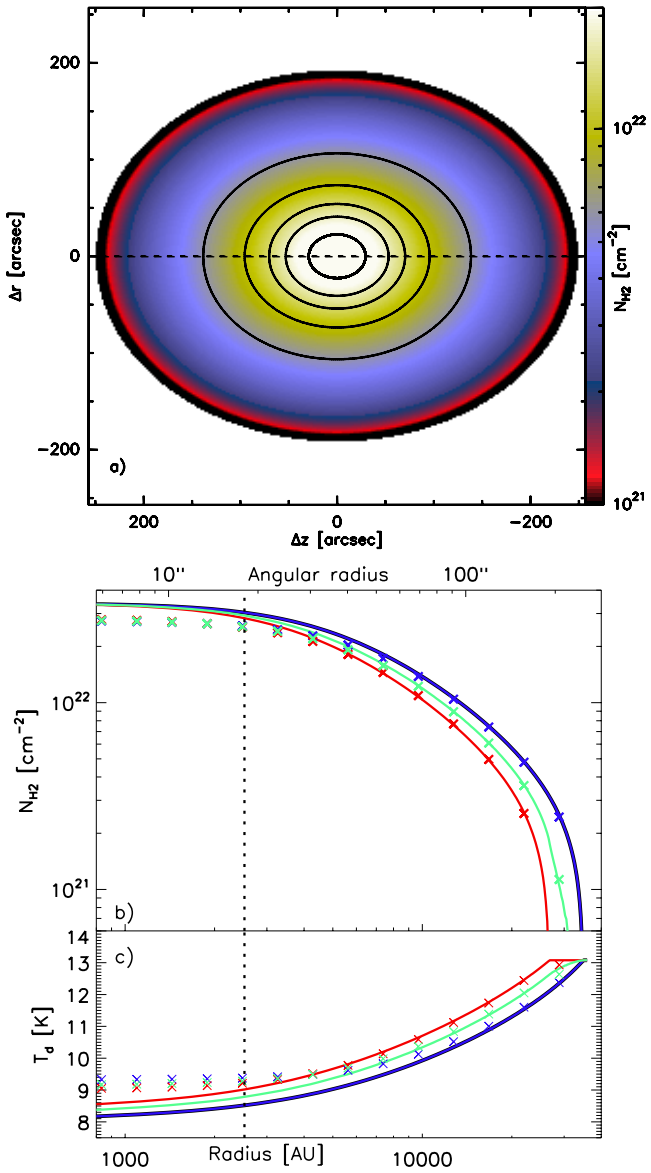

Fig. B.2. a) Synthetic column density image of a prolate ellipsoidal core model with an aspect ratio of 1.3 and a Plummer-like density distribution (see Eq. (B.4) and the text for model parameters). The horizontal dotted line shows the axis of symmetry in the plane of sky, and the contour levels are the same as in Fig. 3. **b)** Comparison between the intrinsic (solid curves) and the reconstructed (crosses) column density profiles of the model. **c)** Comparison between the intrinsic (solid curves) and the reconstructed (crosses) dust temperature profiles of the model. The blue and red curves represent the intrinsic radial profiles along and perpendicular to the axis of symmetry, respectively. The green curves represent the intrinsic circularly averaged radial profiles. The blue and red crosses display the results of the Abel-inversion method applied to the synthetic 160–500 μm intensity profiles of the model, which are convolved to 36.″3 resolution and taken along the major and minor axes, respectively. The green crosses show the reconstruction results by using the circularly averaged intensity profiles of the model as inputs. Note the good agreement between the reconstructed profiles and the intrinsic profiles beyond the half power beam radius of 36.″3/2, as marked by the vertical dotted line.

with L1689B (see Figs. 3 and B.2a), we adopted physical parameters approximately consistent with the observed characteristics of the L1689B core (see Sect. 4.2): central H_2 number density $n_c = 2 \times 10^5$ cm^{-3}; aspect ratio $Z_{flat}/R_{flat} = Z_{out}/R_{out} = 1.3$; flat inner radius along the minor axis $R_{flat} = 4000$ AU; and outer radius along the minor axis $R_{out} = 6.7 \times R_{flat} = 26\,800$ AU.

Because of the lack of spherical symmetry, we applied our Abel reconstruction scheme to three sets of intensity profiles: 1) the profiles measured along the major axis of the model (intrinsic profiles shown as blue curves and results as blue crosses in Fig. B.2); 2) the profiles measured along the minor axis of the model (intrinsic profiles shown as red curves and results as red crosses in Fig. B.2); and 3) circularly averaged intensity profiles (intrinsic profiles shown as green curves and results as green crosses in Fig. B.2). Here, again, it can be seen that the reconstruction results are very satisfactory (2% agreement) beyond the beam radius (marked by the vertical dotted line in Fig. B.2). The reconstruction performed perpendicular to the axis of symmetry, i.e., along the minor axis for a prolate core, is more accurate (1%) than the reconstruction performed along the axis of symmetry (4%). In particular, the best estimate of the central dust temperature is obtained from the reconstruction performed along the minor axis. The reconstruction along the major axis nevertheless provides better estimates of the column density and temperature at large radii along the major axis. The central column density reconstructed at 500 μm resolution slightly underestimates but still agrees to within 20% with the true column density at core center. The best estimate of the total core mass, as obtained by using the results of the reconstruction performed on the circularly averaged intensity profiles, agrees more accurate than 4% with the model core mass. Even for a more elongated core model with an aspect ratio of 2 (instead of 1.3), the reconstructed core mass still agrees with the model mass to within 5%.

We also performed similar simulations for an oblate core model observed edge-on. The accuracy of the reconstruction results was found to be essentially the same as for the prolate case. Again, the reconstruction performed perpendicular to the axis of symmetry, i.e., along the major axis in this case, was found to be more accurate than the reconstruction performed along the axis of symmetry. The best estimate of the total core mass was again obtained from reconstructing the circularly averaged intensity profiles.